



This is a repository copy of *Magnetohydrodynamic wave modes of solar magnetic flux tubes with an elliptical cross section.*

White Rose Research Online URL for this paper:
<https://eprints.whiterose.ac.uk/174741/>

Version: Published Version

Article:

Aldhafeeri, A.A., Verth, G., Brevis, W. et al. (3 more authors) (2021) Magnetohydrodynamic wave modes of solar magnetic flux tubes with an elliptical cross section. *The Astrophysical Journal*, 912 (1). 50. ISSN 0004-637X

<https://doi.org/10.3847/1538-4357/abec7a>

Reuse

This article is distributed under the terms of the Creative Commons Attribution (CC BY) licence. This licence allows you to distribute, remix, tweak, and build upon the work, even commercially, as long as you credit the authors for the original work. More information and the full terms of the licence here:
<https://creativecommons.org/licenses/>

Takedown

If you consider content in White Rose Research Online to be in breach of UK law, please notify us by emailing eprints@whiterose.ac.uk including the URL of the record and the reason for the withdrawal request.



eprints@whiterose.ac.uk
<https://eprints.whiterose.ac.uk/>



Magnetohydrodynamic Wave Modes of Solar Magnetic Flux Tubes with an Elliptical Cross Section

Anwar A. Aldhafeeri^{1,2}, Gary Verth¹, Wernher Brevis³, David B. Jess⁴, Max McMurdo¹, and Viktor Fedun⁵

¹ Plasma Dynamics Group, School of Mathematics and Statistics, University of Sheffield, Hicks Building, Hounsfield Road, Sheffield S3 7RH, UK
aaaldhafeeri1@sheffield.ac.uk, aaaldhafeeri@kfu.edu.sa

² Mathematics and Statistic Department, Faculty of Science, King Faisal University, Al-Hassa, P.O. Box 400, Hofuf 31982, Saudi Arabia

³ Departamento de Ingeniería Hidráulica y Ambiental and Departamento de Minería, Pontificia Universidad Católica de Chile, Santiago 3580000, Chile

⁴ Astrophysics Research Centre, School of Mathematics and Physics, Queen's University Belfast, Belfast BT7 1NN, UK

⁵ Plasma Dynamic Group, Department of Automatic Control and Systems Engineering, The University of Sheffield, Mappin Street, Sheffield S1 3JD, UK

Received 2020 October 3; revised 2021 March 2; accepted 2021 March 5; published 2021 May 4

Abstract

The purpose of this paper is to study the behavior of magnetohydrodynamic (MHD) wave modes that propagate in compressible magnetic flux tubes with an elliptical cross section embedded in a magnetic environment. The dispersion relation that describes the behavior of MHD wave modes permitted in an elliptical magnetic flux tube is solved numerically. Distortion of the spatial structure of the purely real eigenmodes from the well-known circular flux tube model has been considered. It has been studied under both photospheric and coronal conditions. It has been shown that (i) solutions in the form of even Mathieu functions are more sensitive to the value of eccentricity than solutions with the form of odd Mathieu functions; (ii) if the ellipticity of the cross section of the magnetic flux tube increases, a sausage mode ($m = 0$) cannot be easily identified; (iii) even solutions that correspond to the fluting mode ($m = 3$) can be misinterpreted as a kink mode ($m = 1$) due to their similarities. In contrast to the fluting modes that are polarized along the major axis and strongly depend on the ellipticity of the magnetic flux tube, the kink and sausage surface modes are practically unaffected by ellipticity. Several examples of the spatial structure of the eigenmodes permitted in the pores and sunspots have been visualized. The solutions obtained in the approximation of cylindrical symmetry are in agreement with previous studies.

Unified Astronomy Thesaurus concepts: [Magnetohydrodynamics \(1964\)](#); [Solar photosphere \(1518\)](#); [Solar corona \(1483\)](#)

1. Introduction

The high-resolution ground and space-based observations of the solar atmosphere in combination with the theory of magnetohydrodynamic (MHD) wave propagation provides us with an opportunity to understand the behavior of observed waves in more detail. Since the discovery of Alfvén (1942) that states that plasma supports wave-like variation in the magnetic field, much research effort has been devoted to the study of MHD wave oscillations in the solar atmosphere under a variety of plasma parameters and different magnetic structures. MHD wave propagation in unbounded homogeneous plasma has previously been analyzed by many researchers such as Lighthill (1960), Cowling (1976), Parker (2004), Goedbloed & Poedts (2004), Aschwanden (2005), and Priest (2014).

MHD wave propagation in a bounded inhomogeneous plasma configuration has been extensively studied in the past (see, e.g., Verth & Erdélyi 2008; Goossens et al. 2014, 2019; Jess et al. 2015; Verth & Jess 2016; Cheremnykh et al. 2017, 2018; Magyar et al. 2019). Verth & Erdélyi (2008) investigated the effect of an inhomogeneous magnetic field on coronal loop oscillations. The effects caused by the presence of a magnetic twist in cylindrical flux tubes have been studied by Fedun (2008). Goossens et al. (2014) studied the kink wave in solar magnetic flux tubes and found that the velocity field of the kink wave is naturally a sum of both transverse and

rotational motion. Jess et al. (2015) reviewed the characterization and interpretation of oscillations that appear in the solar chromosphere.

A variety of analytical models have been used to analyze wave propagation in the magnetic interface (Wentzel 1979; Roberts 1981a; Musielak et al. 2000; Ballai et al. 2011; Vickers et al. 2018) and slab (Parker 1974; Cram & Wilson 1975; Roberts 1981b; Hornsey et al. 2014; Pascoe & Nakariakov 2016; Mather et al. 2018). Magnetic cylinders with a vertical magnetic field have been studied by Edwin & Roberts (1983), Verth (2007), and Jess et al. (2015), and for the case of a twisted magnetic field, by Ruderman et al. (2014), Giagkiozis et al. (2016), Williams et al. (2016), and Erdélyi & Fedun (2006, 2007, 2010). In particular, Wentzel (1979) investigated the effect of compressibility on the propagation of surface waves at a single interface and derived an expression for the energy carried by such waves. The author has obtained the dispersion relation for the isothermal plasma disturbances without analysis of solutions. Later, Roberts (1981a) provided a more general study of MHD waves behavior at the magnetic interface and analyzed propagation of slow surface waves when one side of the interface is magnetically free. It was shown that “trapped” surface waves have the general property that their wave amplitude, and therefore, their energy decreases with distance from the magnetic interface. Ballai et al. (2011) investigated the nature of globally propagating waves at the spherical interface under solar corona conditions and showed that the frequency of waves increases as the density of plasma decreases at the interface.



Original content from this work may be used under the terms of the [Creative Commons Attribution 4.0 licence](#). Any further distribution of this work must maintain attribution to the author(s) and the title of the work, journal citation and DOI.

In relation to MHD wave propagation in slab geometry, Parker (1974) described the occurrence of surface waves in the isolated slab for the incompressible plasma approximation. Cram & Wilson (1975) studied wave propagation in a compressible slab. The authors showed that fast MHD waves are not free modes of the slab. Roberts (1981b) found that the results of Cram & Wilson (1975) are applicable only if the magnetic slab has a temperature that is higher than its field-free environment. Roberts (1981b) obtained the dispersion relation governing MHD wave propagation in an isolated magnetic slab and specified two main magneto-acoustic modes; the sausage and the kink. These have various subcategories, e.g., slow/fast body and surface waves. The fast magneto-acoustic wave propagates only if the magnetic slab temperature is less than or equal to the temperature of the field-free environment. Furthermore, Roberts (1981b) investigated the wave propagation in the slender slab and found that the kink mode may exist in this regime as well, i.e., when the width of the waveguide is much less than the longitudinal wavelength. Interestingly, under these conditions, the sausage mode can be either a body or surface wave with a phase speed that is close to the tube speed.

Edwin & Roberts (1983) proposed a simple but instructive model for the analysis of MHD wave propagation in magnetic flux tubes that is based on cylindrical geometry. In spite of the complexity of realistic magnetic configurations, many previous studies have been focused on studying the behavior of waves in the magnetic cylinder under different conditions. For example, Erdélyi & Fedun (2007) analyzed the effect of compressible magnetically twisted flux tubes on MHD sausage waves. The authors found that the period of sausage mode oscillations depends on the magnetic twist. More studies in categorizing and interpreting wave propagation in the solar chromosphere were reviewed by Jess et al. (2015). Verth (2007) showed that the frequency and amplitude of the standing fast kink mode can provide us with information regarding the density and magnetic structure of coronal loops.

Ruderman (2003) studied the resonant damping of oscillations of coronal loops with elliptical cross sections under the assumption of zero plasma- β . Erdélyi & Morton (2009) studied wave propagation in the compressible magnetic flux tube with an elliptical cross section when finite plasma- β is considered. It was found that the thin flux tube approximation supports the slow sausage and the fast body mode. Under coronal conditions, the slow and fast body waves for both kink and sausage modes were present, while under photospheric conditions the slow body waves and fast surface waves for kink and sausage modes were present.

Despite the fact that the high-resolution ground-based observations show a great variety of sunspots, a number of studies have been devoted to the analysis of the plasma behavior in a magnetic waveguide with an elliptical cross section. For instance, Liu et al. (2016) studied the flare-induced rotation of a sunspot with an elliptical shape. Also, observational evidence of elliptic pores has been shown by Keys et al. (2018).

It is well known that sunspots and pores do not have an ideal circular cross-sectional shape, see Figure 1, for example. As a result, any imbalance in the diameter of the waveguide requires the use of an elliptical coordinate system instead of a cylindrical one. In this paper, we attempt to analyze the MHD modes permitted in the elliptical magnetic flux tubes.

The corresponding dispersion relation has been solved numerically under both photospheric and coronal conditions. In our model, uniformity along the axis of the magnetic flux tube with an elliptical cross section has been assumed.

Leaky waves give rise to an entirely different mathematical problem and hence will not be addressed in this paper. One must consider either the MHD variables to be complex or compute the solutions numerically as an initial value problem. It will be shown how the spatial structure of the purely real eigenmodes are distorted from the well-known circular flux tube model when an elliptical cross section is considered. Previously, in cylindrical geometry the leaky waves have been explored theoretically by Wilson (1981), Spruit (1982), Cally (1986), Ruderman & Roberts (2006), and Terradas et al. (2007). These waves have also been studied in application to other geometries, e.g., at a single density interface (Vickers et al. 2018), on coronal slabs (Terradas et al. 2005), and on the excitation of leaky modes in cylindrical loops (Terradas et al. 2007).

This paper is tailored to identifying wave modes in pores and sunspots that can be closely approximated with elliptical cross sections. From observational data (see, e.g., Jess et al. 2017; Kang et al. 2019; Albidah et al. 2021) we are restricted to an analysis of the spatial structure of the oscillations inside the umbral regions of pores and sunspots only. The oscillatory signal decays too rapidly outside of these regions to analyze with any certainty. Hence, this indicates that we are observing slow mode type wave modes (which do not strongly perturb the boundary). From a modeling point of view, the difference in external/internal values of magnetic field strength and density only affects the decay rate length scale of the oscillation outside of the waveguide. The internal spatial structure of the mode is largely unaffected and is not of primary interest for the purposes of this paper.

This paper is structured as follows: In Section 2, we derive the general dispersion relation that describes the linear magneto-acoustic waves in a compressible magnetic flux tube with an elliptical cross section. In Section 3, the numerical solutions of this relation obtained under coronal and photospheric conditions are analyzed. In Section 4, we conclude with our results.

2. General Dispersion Relation

Let us consider a straight magnetic flux tube ($\mathbf{B}_{0i} = B_{0i} \mathbf{z}$) with an elliptical cross section embedded in a uniform external magnetic field ($\mathbf{B}_{0e} = B_{0e} \mathbf{z}$). Here, \mathbf{z} is the unit vector parallel to the flux tube axis. The index 0 corresponds to the unperturbed equilibrium state; all dependent variables inside the flux tube are denoted by index i , while quantities outside the tube are denoted by index e . The cross section of the flux tube, perpendicular to its axis, is most conveniently described by the elliptic coordinate system (s, ϕ) shown in Figure 2. The flux tube boundary is defined by the confocal ellipse s_0 (see the blue line in Figure 2).

The well-known equation governing small-amplitude MHD waves, obtained by linearizing the ideal MHD equations (see, e.g., Lighthill 1960; Cowling 1976; Roberts 1981a; Aschwanden 2005), is

$$\frac{\partial^4 \Delta}{\partial t^4} - (c_S^2 + v_A^2) \frac{\partial^2}{\partial t^2} \nabla^2 \Delta + c_S^2 v_A^2 \frac{\partial^2}{\partial z^2} \nabla^2 \Delta = 0, \quad (1)$$

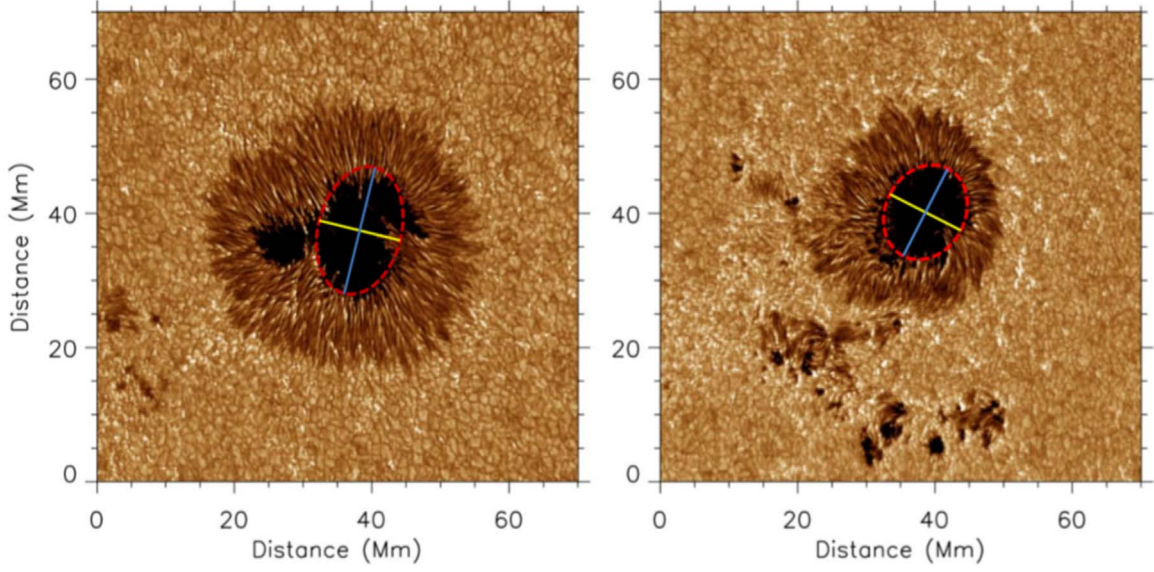


Figure 1. Two active regions, NOAA AR12565 (left panel) and NOAA AR12149 (right panel), captured in the G band by the rapid oscillations in the solar atmosphere (see, e.g., Jess et al. 2010) instrument at the Dunn Solar Telescope. Each panel shows a non-circularly symmetric sunspot structure, highlighting the existence of elliptical magnetic field concentrations in the solar atmosphere. The eccentricity of the image on the left is 0.76 and the image on the right is 0.58.

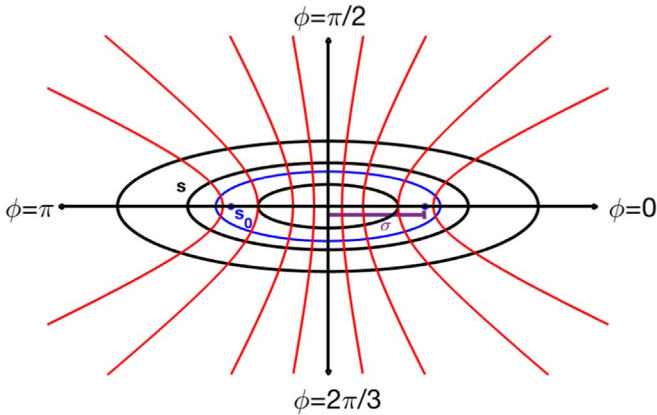


Figure 2. A sketch of the elliptic coordinate system in the x, y plane that is perpendicular to the magnetic flux tube axis. The elliptic coordinates are (s, ϕ) , where s is a non-negative real number and $\phi \in [0, 2\pi]$. The confocal ellipses are shown as contours of constant s and the orthogonal hyperbolas correspond to the constant ϕ contours. The blue confocal ellipse s_0 shows the boundary of the magnetic flux tube. The distance between the center of the ellipse and the focal points is σ .

where

$$\Delta = \nabla \cdot \mathbf{v}, \quad v_A = \frac{B_0}{\sqrt{\mu_0 \rho_0}}, \quad c_S = \sqrt{\gamma \frac{p_0}{\rho_0}}.$$

Here, Δ is the divergence of velocity perturbation \mathbf{v} , v_A is the Alfvén speed, c_S is the sound speed, μ_0 is the magnetic permeability, γ is the ratio of specific heats, p_0 is the unperturbed kinetic plasma pressure, and ρ_0 is the unperturbed plasma density. In the elliptic cylindrical coordinate system (s, ϕ, z) the Laplacian operator can be represented as

$$\nabla^2 = H^{-2} \left(\frac{\partial^2}{\partial s^2} + \frac{\partial^2}{\partial \phi^2} \right) + \frac{\partial^2}{\partial z^2}, \quad (2)$$

where

$$H^2 = \sigma^2 (\sinh^2(s) + \sin^2(\phi)) \quad (3)$$

is a scale factor and σ is the distance between the center of the ellipse and its focal points (see Figure 2). In relation to the Cartesian coordinate system

$$x = \sigma \cosh(s) \cos(\phi), \quad y = \sigma \sinh(s) \sin(\phi),$$

where the x -axis is directed along the major axis of the ellipse and the y -axis is directed along the minor axis.

By applying Fourier decomposition and separation of variables the solution of Equation (1) can be represented as

$$\Delta = S(s) \Phi(\phi) \exp(i(kz - \omega t)), \quad (4)$$

where k is the wavenumber in the z direction, ω is the angular frequency, and the functions $S(s)$ and $\Phi(\phi)$ are to be determined. By substituting Equation (4) into Equation (1), the perturbed components of velocity \mathbf{v} , magnetic field \mathbf{b} , pressure p , and total pressure p_T in the elliptic coordinate system can be derived explicitly as (see, e.g., Erdélyi & Morton 2009)

$$v_s(s, \phi) = - \left(\frac{\omega^2 - k^2 c_S^2}{H \omega^2 m_0^2} \right) \frac{\partial S(s)}{\partial s} \Phi(\phi),$$

$$v_\phi(s, \phi) = - \left(\frac{\omega^2 - k^2 c_S^2}{H \omega^2 m_0^2} \right) S(s) \frac{\partial \Phi(\phi)}{\partial \phi},$$

$$v_z(s, \phi) = - \left(\frac{i k c_S^2}{\omega^2} \right) S(s) \Phi(\phi),$$

$$b_s(s, \phi) = B_0 \frac{k}{\omega} v_s(s, \phi),$$

$$b_\phi(s, \phi) = -B_0 \frac{k}{\omega} v_\phi(s, \phi),$$

$$b_z(s, \phi) = -i B_0 \frac{\omega^2 - k^2 c_S^2}{\omega^3} S(s) \Phi(\phi),$$

$$p(s, \phi) = -i\rho_0 \frac{c_S^2}{\omega} S(s) \Phi(\phi),$$

$$p_T(s, \phi) = -\frac{i\rho_0}{\omega^3} (c_S^2 + v_A^2) (\omega^2 - k^2 c_T^2) S(s) \Phi(\phi),$$

$$\rho(s, \phi) = -\frac{i\rho_0}{\omega} S(s) \Phi(\phi).$$

Here, v_s , v_ϕ , and v_z are the perturbed velocity components in the s , ϕ , and z directions, respectively; b_s , b_ϕ , and b_z are the perturbed magnetic field components; p is the plasma pressure perturbation; p_T is the total plasma pressure perturbation, i.e., the sum of kinetic and magnetic plasma pressures; and ρ is the plasma density perturbation.

It is clear that the density perturbation is proportional to other MHD variables. Note that all other components are proportional to the same functions.

Equation (1) can be represented in an elliptic cylindrical coordinate system by substituting ∇^2 from Equation (2) and Δ from Equation (4) into Equation (1). It is shown to be

$$H^{-2} \left(\frac{1}{S} \frac{\partial^2 S}{\partial s^2} + \frac{1}{\Phi} \frac{\partial^2 \Phi}{\partial \phi^2} \right) + \frac{4}{\sigma^2} m_0^2 = 0, \quad (5)$$

where

$$m_0^2 = \frac{\sigma^2 (\omega^2 - k^2 c_S^2) (\omega^2 - k^2 v_A^2)}{4 (c_S^2 + v_A^2) (\omega^2 - k^2 c_T^2)} \quad (6)$$

and the tube speed is given by

$$c_T^2 = \frac{c_S^2 v_A^2}{c_S^2 + v_A^2}. \quad (7)$$

By substituting Equation (3) into the Equation (5), Equation (5) can be rewritten as

$$\frac{1}{S} \frac{\partial^2 S}{\partial s^2} + 4m_0^2 \sinh^2(s) = - \left(\frac{1}{\Phi} \frac{\partial^2 \Phi}{\partial \phi^2} + 4m_0^2 \sin^2(\phi) \right). \quad (8)$$

Introducing the separation constant, h , Equation (8) can be rewritten as two ordinary differential equations, where h is a constant to be determined. These two equations are

$$\frac{d^2 \Phi}{d\phi^2} + (h - 2m_0^2 \cos(2\phi)) \Phi = 0 \quad (9)$$

and

$$\frac{d^2 S}{ds^2} - (h - 2m_0^2 \cosh(2s)) S = 0. \quad (10)$$

In the case where h and m_0 are real and $m_0^2 > 0$, Equations (9) and (10) represent the Mathieu equation and modified Mathieu equation, respectively (see, e.g., Mathieu 1868; Morse & Feshbach 1953; Bateman 1955; Abramowitz & Stegun 1964; National Institute of Standards and Technology (NIST; 2020).

The sign of m_0^2 is dependent on the coordinate system in use. Under elliptical coordinates, m_0^2 has the opposite sign of m_0^2 under cylindrical coordinates, i.e., $\frac{4}{\sigma^2} m_0^2$ in elliptical coordinates is equal to $-m_0^2$ in cylindrical coordinates (see, e.g., Spruit 1982; Edwin & Roberts 1983).

In order to obtain the periodic solution of the Mathieu equation, the particular value of m_0^2 should be suitably related

Table 1

The Permitted Combination of the Indices of the Radial Mathieu Function with Respect to the Major Axis (Even Solution), $C_m(s, m_0^2)$ and Minor Axis (Odd Solution), $S_m(s, m_0^2)$

m	C_{2n}	S_{2n}
0	$n = 0$	n/a
2	$n = 1$	$n = 1$
4	$n = 2$	$n = 2$
6	$n = 3$	$n = 3$
:	:	:

Note. $m = 2n + j$ is the order of the Mathieu function and $j = 0$ corresponds to the even order of the Mathieu function. For the odd Mathieu function of even order, n starts from 1, and therefore, the case $m = 0$ for S_{2n} cannot be realized.

Table 2

The Permitted Combination of the Radial Mathieu Function Indices with Respect to the Major Axis (Even Solution), $C_m(s, m_0^2)$ and Minor Axis (Odd Solution), $S_m(s, m_0^2)$

m	C_{2n+1}	S_{2n+1}
1	$n = 0$	$n = 0$
3	$n = 1$	$n = 1$
5	$n = 2$	$n = 2$
7	$n = 3$	$n = 3$
:	:	:

Note. $m = 2n + j$ is the order of the Mathieu function and $j = 1$ corresponds to the odd order of the Mathieu function.

to the parameter h , which has an infinite set of distinct values (see Appendix A for more detail). The Mathieu equations have odd solutions with respect to the minor axis denoted by $S_{2n+j}(s, m_0^2)$ for radial Mathieu functions and $s_{2n+j}(\phi, m_0^2)$ for angular Mathieu functions. The even solutions with respect to the major axis are denoted by $C_{2n+j}(s, m_0^2)$ for radial Mathieu functions and $c_{2n+j}(\phi, m_0^2)$ for angular Mathieu functions (see, e.g., McLachlan 1947), where $n \in \mathbb{N}$ and $j = 0, 1$. See Tables 1 and 2 for more details.

The magnitude of m_0 plays a crucial role in determining how much the confocal ellipse node is of the modes. There is an infinite set of possible values of m_0 that satisfy the boundary conditions. On the other side, even and odd Mathieu functions have an even and odd order, which corresponds to the different hyperbola nodes (see Figure 2). In an elliptical coordinate system, the modified Mathieu function Equation (10), is the solution of the radial Mathieu equation and corresponds to the Bessel equation in polar coordinates. When $m_0^2 > 0$, the solutions of Equation (10) are oscillatory radial Mathieu functions, which can be represented as a series of Bessel functions of first kind (J_m) (see Appendix B). This provides the internal part of the solutions for body modes (Section 2.1).

When $m_0^2 < 0$, Equation (10) becomes

$$\frac{d^2 S}{ds^2} - (h + 2m_0^2 \cosh(2s)) S = 0. \quad (11)$$

The solutions are non-oscillatory radial Mathieu functions, which can be represented as a series of modified Bessel functions of the first kind (I_m). These provide the internal part

of the solutions for surface modes (Section 2.1). When $m_e^2 < 0$, there are also evanescent modified Mathieu functions of the third kind, which can be written as a series of modified Bessel functions of the second kind (K_m) and the first kind (I_m) (see Appendix D). These functions correspond to the external part of the solutions for both body and surface modes (see Section 2.2).

2.1. The General Solution Inside the Magnetic Flux Tube

The even and odd solutions of Equations (10) and (11), confined within the flux tube boundary confocal ellipse, s_0 ($s < s_0$), are

$$\Delta_i = S(s)\Phi(\phi) = \begin{cases} A_0 C_{2n+j}(s, m_{0i}^2) c_{2n+j}(\phi, m_{0i}^2) & \text{even,} \\ B_0 S_{2n+j}(s, m_{0i}^2) s_{2n+j}(\phi, m_{0i}^2) & \text{odd.} \end{cases} \quad (12)$$

Here, A_0 and B_0 are arbitrary constants and

$$m_{0i}^2 = \frac{\sigma^2 (\omega^2 - k^2 c_{Si}^2)(\omega^2 - k^2 v_{Ai}^2)}{4 (c_{Si}^2 + v_{Ai}^2)(\omega^2 - k^2 c_{Ti}^2)}.$$

Let us introduce notation for the internal body mode solutions as Θ_m^E and Θ_m^O , where the superscripts E and O denote the even and odd solutions, respectively. The subscript m relates the elliptical wave modes to the cylindrical wave modes, i.e., sausage ($m = 0$), kink ($m = 1$), and fluting modes ($m \geq 2$), see Tables 1 and 2 for more details.

When $m_{0i}^2 > 0$, the internal even and odd body mode solutions are

$$\Theta_m^E(m_{0i}, s) = C_{2n+j}(s, m_{0i}^2), \quad (13)$$

$$\Theta_m^O(m_{0i}, s) = S_{2n+j}(s, m_{0i}^2). \quad (14)$$

Here, the even and odd internal surface mode solutions are denoted as Ξ_m^E and Ξ_m^O , respectively. When $m_{0i}^2 < 0$ the internal surface mode solutions are

$$\Xi_m^E(|m_{0i}|, s) = C_{2n+j}(s, m_{0i}^2), \quad (15)$$

$$\Xi_m^O(|m_{0i}|, s) = S_{2n+j}(s, m_{0i}^2). \quad (16)$$

Θ and Ξ can be represented in the form of series of Bessel functions, J_m and I_m (see Appendices B, C, and D). The solutions in the form of Bessel functions is more convenient for numerical calculations.

2.2. The General Solution Outside the Magnetic Flux Tube

For $m_e^2 < 0$ in the external region, ($s > s_0$) the amplitude of the non-oscillatory perturbations decay with distance from the magnetic flux tube and therefore

$$\Delta_e = S(s)\Phi(\phi) = \begin{cases} A_e FeK_{2n+j}(s, m_{0e}^2) c_{2n+j}(\phi, m_{0e}^2) & \text{even,} \\ B_e GeK_{2n+j}(s, m_{0e}^2) s_{2n+j}(\phi, m_{0e}^2) & \text{odd,} \end{cases} \quad (17)$$

where

$$m_{0e}^2 = \frac{\sigma^2 (\omega^2 - k^2 c_{Se}^2)(\omega^2 - k^2 v_{Ae}^2)}{4 (c_{Se}^2 + v_{Ae}^2)(\omega^2 - k^2 c_{Te}^2)}.$$

A_e and B_e are the arbitrary constants and $FeK_{2n+j}(s, m_{0e}^2)$ and $GeK_{2n+j}(s, m_{0e}^2)$ are the modified Mathieu functions of the third kind. Let us introduce the notation for the even and odd external evanescent solutions as Ψ_m^E and Ψ_m^O , respectively,

$$\Psi_m^E(|m_{0e}|, s) = FeK_{2n+j}(s, m_{0e}^2),$$

$$\Psi_m^O(|m_{0e}|, s) = GeK_{2n+j}(s, m_{0e}^2).$$

2.3. The General Dispersion Relation

To obtain the general dispersion relation, the total pressure balance has to be satisfied, i.e.,

$$p_{0i} + \frac{B_{0i}^2}{2\mu_0} = p_{0e} + \frac{B_{0e}^2}{2\mu_0}. \quad (18)$$

Here, p_{0i} and p_{0e} are the plasma pressures inside and outside of the magnetic flux tube, and B_{0i} and B_{0e} are the magnetic fields in the corresponding regions.

By taking into account the continuity of the velocity v_s and total plasma pressure (p_T) across the boundary of magnetic flux tube $s = s_0$ (see, e.g., Equation (18)), the dispersion relations for body modes ($m_{0i}^2 > 0$) are found to be

$$\begin{aligned} & \frac{v_{ph}^2 - c_{Si}^2}{m_{0i}^2 v_{ph}^2} M_{0e} \frac{\Theta_m^{E,O}(m_{0i}, s_0)}{\Theta_m^{E,O}(m_{0i}, s_0)} \\ &= \frac{v_{ph}^2 - c_{Se}^2}{m_{0e}^2 v_{ph}^2} M_{0i} \frac{\Psi_m^{E,O}(|m_{0e}|, s_0)}{\Psi_m^{E,O}(|m_{0e}|, s_0)} \end{aligned} \quad (19)$$

and for the surface modes ($m_{0i}^2 < 0$)

$$\begin{aligned} & \frac{v_{ph}^2 - c_{Si}^2}{m_{0i}^2 v_{ph}^2} M_{0e} \frac{\Xi_m^{E,O}(|m_{0i}|, s_0)}{\Xi_m^{E,O}(|m_{0i}|, s_0)} \\ &= \frac{v_{ph}^2 - c_{Se}^2}{m_{0e}^2 v_{ph}^2} M_{0i} \frac{\Psi_m^{E,O}(|m_{0e}|, s_0)}{\Psi_m^{E,O}(|m_{0e}|, s_0)}, \end{aligned} \quad (20)$$

where $v_{ph} = \frac{\omega}{k}$ is the phase speed, and

$$M_{0i} = \rho_{0i} (c_{Si}^2 + v_{Ai}^2) (c_{Ti}^2 - v_{ph}^2),$$

$$M_{0e} = \rho_{0e} (c_{Se}^2 + v_{Ae}^2) (c_{Te}^2 - v_{ph}^2).$$

The prime in Equations (19) and (20) denotes the derivative of the Mathieu function with respect to the confocal ellipse curve, s .

3. MHD Wave Modes under Coronal and Photospheric Conditions

The dispersion relation Equations (19) and (20) under coronal and photospheric conditions is solved numerically. The set of solutions were obtained under coronal conditions: (i) the slow kink and sausage body modes with a phase speed ranging between internal tube speed c_{Ti} and internal sound speed c_{Si} , (ii) fast kink and sausage body modes with a phase speed ranging between internal Alfvén speed v_{Ai} and external Alfvén speed v_{Ae} ; under photospheric conditions (iii) the slow kink and sausage surface modes, and slow kink and sausage body modes have phase speeds between c_{Ti} and c_{Si} , (iv) the fast kink and sausage surface modes with a phase speed between v_{Ai} and v_{Ae} (see Appendix E for more detail). It was also found that

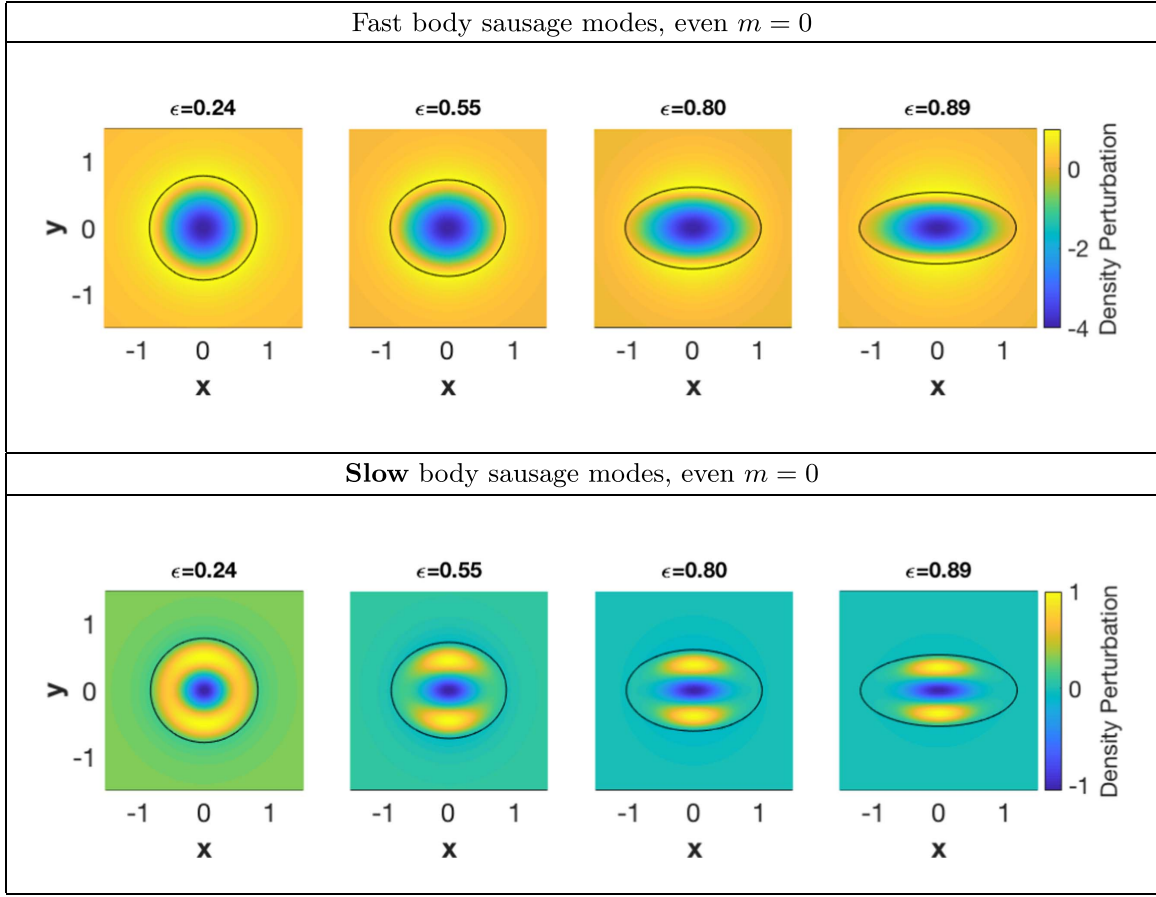


Figure 3. The normalized density perturbation calculated under coronal conditions, i.e., $v_{Ae}, v_{Ai} > c_{Si}, c_{Se}$ for the different values of eccentricity. The upper panel shows the fast branch of the sausage mode, which has no hyperbola node and no ellipse node. The lower panel shows the slow branch of sausage mode, which has no hyperbola node and one ellipse node, i.e., the even solution of the Mathieu equation. $m = 0$ represents the order of the Bessel function.

eccentricity

$$\epsilon = \frac{1}{\cosh(s_0)} \quad (21)$$

has a strong effect on the solution behavior. In particular, as the ellipticity of the cross section increases, the difference in the phase speeds of two kink modes that polarized along the major axis and the minor axis also increase. If the ellipticity decreases, e.g., in the approximation of a circle-like shape, our results agree with the results obtained previously by Erdélyi & Morton (2009). In the following sections we discuss the obtained mode patterns and the effect of ellipticity on MHD modes in more detail.

3.1. Coronal Conditions

To satisfy coronal conditions, it is assumed that the internal plasma temperature, density, and pressure are greater than at the external region and the internal magnetic field strength is less than external magnetic field strength. This corresponds to the following relationships between the characteristic plasma speeds: $c_{Si} = 1$, $v_{Ae}, v_{Ai} > c_{Si}, c_{Se}$. The chosen conditions are required for slow and fast body waves to occur. Therefore, if we choose $v_{Ai} > v_{Ae}$, fast body waves are absent and only two of the infinitely many slow body waves are shown (a further explanation can be found in Roberts 1981b and Edwin & Roberts 1983). The wave solutions must satisfy the physical

Table 3
The Symmetrical Properties of the Mathieu Functions

Mathieu Function	Order	Major Axis	Minor Axis
Even	Even	Symmetrical	Symmetrical
Even	Odd	Symmetrical	Asymmetrical
Odd	Even	Asymmetrical	Asymmetrical
Odd	Odd	Asymmetrical	Symmetrical

conditions, whereby the oscillations are mainly confined to the ellipse region and they decay outside of the boundary of the magnetic flux tube. Therefore, m_{0e}^2 should be negative in order to satisfy the evanescent solutions in the external region and m_{0i}^2 should be positive in order to satisfy the oscillation solutions in the internal region. For numerical calculations the following values of the characteristic speeds have been used: $v_{Ae} = 5c_{Si}$, $c_{Se} = 0.5c_{Si}$, and $v_{Ai} = 2c_{Si}$. For this set of chosen parameters the total pressure balance between the internal and external plasma requires $\frac{\rho_e}{\rho_o} = 0.21$.

3.1.1. Sausage Mode

For the sausage modes ($m = 0$), the permitted combinations of the indices of the radial Mathieu function with respect to the major (even solution) and minor (odd solution) axes are shown in Tables 1 and 2. Figure 3 illustrates the density perturbation of the sausage modes by taking into account different

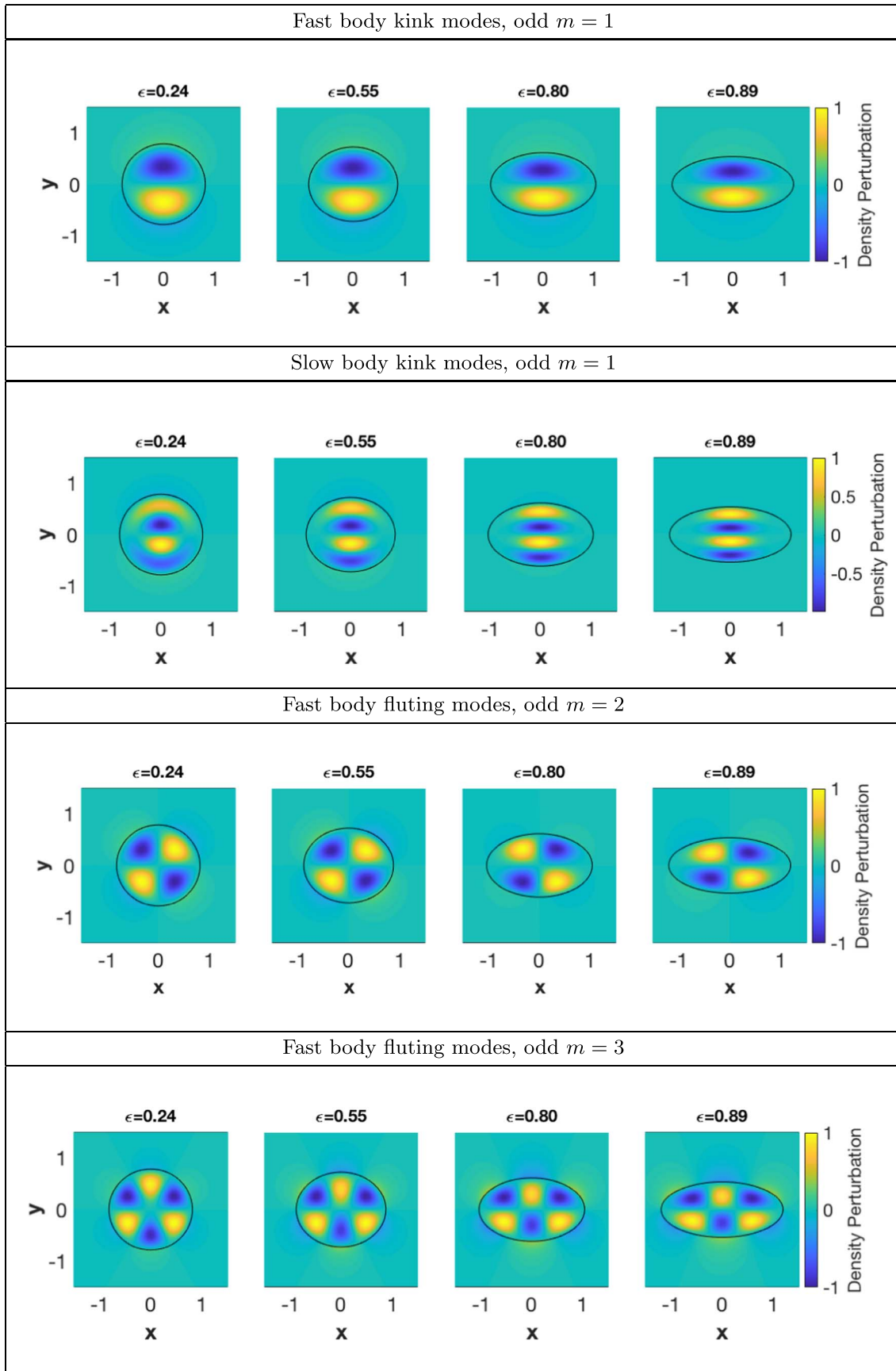


Figure 4. The normalized density perturbations under solar corona conditions, i.e., $v_{Ae}, v_{Ai} > c_{Si}, c_{Se}$ for the different values of eccentricity. From the top to bottom we show the fast branch of the kink mode, which has one hyperbola node and one ellipse node; the fast branch of the kink mode, which has one hyperbola node and two ellipse nodes; the fast branch of the fluting $m = 2$ mode, which has two hyperbola nodes and one ellipse node; the fast branch of the fluting $m = 3$ mode, which has three hyperbola nodes and one ellipse node, i.e., the odd solution of the Mathieu equation (Equations (13)–(16)).

Table 4
Above are the Chosen Values for the Modes Under Coronal Conditions

Sausage Modes								
ϵ	$m = 0$, even (0, 1)		$m = 0$, even (0, 2)		$m = 0$, even (0, 2)		$m = 0$, even (0, 2)	
	k_{s_0}	v_{PH}	k_{s_0}	v_{PH}	k_{s_0}	v_{PH}	k_{s_0}	v_{PH}
0.241	2.98	3.3547	1.01	0.8953
0.55	2.98	3.3807	1.01	0.8952
0.80	2.98	3.5476	1.01	0.8951
0.89	2.98	3.7626	1.01	0.8962
Kink Modes								
ϵ	$m = 1$, even (1, 1)		$m = 1$, odd (1, 1)		$m = 1$, even (1, 2)		$m = 1$, odd (1, 2)	
	k_{s_0}	v_{PH}	k_{s_0}	v_{PH}	k_{s_0}	v_{PH}	k_{s_0}	v_{PH}
0.241	3.99	3.5748	3.99	3.6080	3.99	0.9031	3.99	0.9028
0.55	3.99	3.5108	3.99	3.7100	3.99	0.9030	3.99	0.9020
0.80	3.99	3.4887	3.99	4.0059	3.99	0.9017	3.99	0.9003
0.89	3.99	3.6007	3.99	4.3085	3.99	0.9007	3.99	0.8991
Fluting Modes								
ϵ	$m = 2$, even (2, 1)		$m = 2$, odd (2, 1)		$m = 3$, even (3, 1)		$m = 3$, odd (3, 1)	
	k_{s_0}	v_{PH}	k_{s_0}	v_{PH}	k_{s_0}	v_{PH}	k_{s_0}	v_{PH}
0.241	3.99	4.2523	3.99	4.2556	3.99	4.9322	3.99	4.9325
0.55	3.99	4.1590	3.99	4.2236	3.99	4.8564	3.99	4.9117
0.80	3.99	3.9591	3.99	4.0088	3.99	4.5414	3.99	4.9270
0.89	3.99	3.9012	3.99	3.7333	3.99	4.3602	3.99	4.9807

Note. The wavenumber $k_{s_0} = ke^{s_0}\sigma/2$ is a dimensionless quantity normalized on $e^{s_0}\sigma/2$. The term $e^{s_0}\sigma/2 \rightarrow a$ as $b \rightarrow a$, i.e., our elliptical cross section tends toward a circular cross section when the major and minor axes become equal. The distance between the major axis a and minor axis b are connected by s_0 , so, where s_0 is the specific confocal elliptic cylinder centered on the origin and $\sigma = \sqrt{a^2 - b^2}$, the limit as $s_0 \rightarrow \infty$ corresponds to a magnetic flux tube having a circular cross section. In the opposite limit, where $s_0 \rightarrow 0$, the cross section is shrunk into the interval $[-\sigma, \sigma]$ on the x -axis, that is, the minor axis tends to zero. The distance between the center and foci points, σ is a quantity that represents a length with units of megameters.

eccentricities of the elliptical cross section of the magnetic flux tube. The chosen value used to plot this mode is shown in Table 4. The first panel in Figure 3 shows the fundamental sausage modes. It is clear that as the ellipticity, (ϵ), of the cross section increases, the sausage mode can be identified easier. However, for the case where we have higher order sausage modes (see the second panel in Figure 3), the mode pattern changes in comparison to the pattern of the sausage mode for the circular cross section. As the ellipticity of the cross section increases, the mode pattern of this mode became different from the sausage mode of the flux tube with the circular cross section (see Figure 3). This happens because as the ellipticity of the tube increases, the length of the major axis of the flux tube increases, while the minor axis of the tube shrinks. Therefore, the displacement limitation has to be extended to the first elliptic node along the major axis causing the separation of the displacement that surrounds it. As a result, for clear mode identification, it is necessary to take into account the symmetric properties of the Mathieu functions. Since $c_{2n}(\phi, m_{0i}^2) = c_{2n}(2\pi - \phi, m_{0i}^2)$, when solutions are even functions (the displacement or perturbation is polarized along the major axis) and when they have an even order expressed by $C_{2n}(s, m_{0i}^2)c_{2n}(\phi, m_{0i}^2)$, the displacement will be symmetric about the major and minor axes. Figure 3 shows the symmetric density perturbation with respect to the major and minor axes (see Table 3). The first and second columns in Table 4 reveal the eccentricity, wavenumber, and phase velocity that were

used for visualization of the fast body sausage mode solution under coronal conditions.

3.1.2. Kink Mode

The parameters used to plot the kink mode ($m = 1$) are shown in the Table 4. For this set of parameters, the fast body kink mode is shown in the top panels of Figures 4 and 5, while the slow body kink mode is shown in the second panels of the same figures. Since the displacement could be toward the major minor axes, there are two polarized kink modes in the elliptical flux tube. The Mathieu functions of the even type describe the behavior of the kink mode as a bulk transverse motion along the major axis, while the Mathieu functions of the odd type describe the behavior of the kink mode as a bulk of transverse motion along the minor axis. The first and second panels in Figure 4 illustrate the kink modes polarized along the minor axis for different flux tubes of diverse eccentricity, whereas the first and second panels in Figure 5 illustrate the kink modes polarized along the major axis for the different flux tubes of diverse eccentricity. The first panels in Figures 4 and 5 represent the fundamental kink mode. As the ellipticity, (ϵ), of the cross section of the flux tube increases, the fundamental kink mode can be easily identified for waves polarized along the major and minor axes.

However, as the ellipticity of the cross section of the flux tube increases, the higher order kink mode polarized along the major axis appears similar to a fluting mode $m = 3$, and hence,

Table 5
The Chosen Values for Modes under Photospheric Conditions

Sausage Surface Modes								
$m = 0$, even (0, 1)								
ϵ	k_{s0}	v_{PH}	k_{s0}	v_{PH}	k_{s0}	v_{PH}	k_{s0}	v_{PH}
0.241	2.50	1.4386
0.55	2.50	1.4394
0.80	2.50	1.4449
0.89	2.50	1.4528
Kink Surface Modes								
$m = 1$, even (1, 1)			$m = 1$, odd (1, 1)					
ϵ	k_{s0}	v_{PH}	k_{s0}	v_{PH}	k_{s0}	v_{PH}	k_{s0}	v_{PH}
0.241	2.50	1.3325	2.50	1.3225
0.55	2.50	1.3573	2.50	1.2972
0.80	2.50	1.4091	2.50	1.2417
0.89	2.50	1.4468	2.50	1.1968
Fluting Surface Modes								
$m = 2$, even (2, 1)		$m = 2$, odd (2, 1)		$m = 3$, even (3, 1)		$m = 3$, odd (3, 1)		
ϵ	k_{s0}	v_{PH}	k_{s0}	v_{PH}	k_{s0}	v_{PH}	k_{s0}	v_{PH}
0.241	2.50	1.2856	2.50	1.2854	11.0	1.2741	11.0	1.2597
0.55	2.50	1.2882	2.50	1.2817	11.0	1.2981	11.0	1.1787
0.80	2.50	1.3061	2.50	1.2564	11.0	1.3388	11.0	1.4349
0.89	2.50	1.3308	2.50	1.2207	11.0	1.3747	11.0	1.3636

Note. The notations of the variables are the same as those in Table 4.

could be misinterpreted. The second panel in Figure 5, starting from the left displays a kink mode for the case of the magnetic flux tube close to the circular cross section and as one progresses to the right ends up as a kink mode with $\epsilon = 0.89$, which can lead to a misinterpretation.

Alternatively, as the ellipticity of the cross section of the flux tube increases, the kink overtone mode polarized along the minor axis can be easily identified. $C_{2n+1}(s, m_{0i}^2)c_{2n+1}(\phi, m_{0i}^2)$ represent the solution of the kink waves polarized along major axis. The even and odd solutions of the elliptic modes correspond to the kink mode of the circular membrane. Since $c_{2n+1}(\phi, m_{0i}^2) = -c_{2n+1}(\pi \pm \phi, m_{0i}^2)$, the density perturbation is symmetric about the major axis but it is asymmetric about the minor axis (see the first and second panels in Figure 5). $S_{2n+1}(s, m_{0i}^2)s_{2n+1}(\phi, m_{0i}^2)$ represents the solution of kink waves polarized along the minor axis. Since $s_{2n+1}(\phi, m_{0i}^2) = \mp s_{2n+1}(\pi \pm \phi, m_{0i}^2)$, the density perturbation is asymmetric about the major axis but it is symmetrical with respect to the minor axis, i.e., the first and second panels in Figure 4.

3.1.3. Fluting Modes

For the fluting modes ($m \geq 2$), the values used for visualization are presented in Table 4. The third and fourth panels in Figures 4 and 5 illustrate perturbations along the minor and major axes for different values of eccentricity. From studying the third and fourth panels in Figure 5, it is shown that as the eccentricity of the flux tube increases, the displacements merge. As a result, this may lead to the visual interpretation of these modes as a kink mode ($m = 1$). Note, the waves that perturbed along the minor axis are less affected by the ellipticity, thus, one can clearly observe the fluting modes

($m = 2$) and ($m = 3$) as the eccentricity increases, again, see the third and fourth panels in Figure 4.

For the fluting mode ($m = 2$), $C_{2n}(s, m_{0i}^2)c_{2n}(\phi, m_{0i}^2)$ represents the solution for the perturbation along the major axis. Since $c_{2n}(\phi, m_{0i}^2) = c_{2n}(\pi \pm \phi, m_{0i}^2)$, the density perturbation is symmetric about both axes (see the third panels in Figure 5). $S_{2n+2}(s, m_{0i}^2)s_{2n+2}(\phi, m_{0i}^2)$ represents the solution for perturbation about the minor axis. Since $s_{2n+2}(\phi, m_{0i}^2) = \pm s_{2n+2}(\pi \pm \phi, m_{0i}^2)$, the density perturbation is asymmetric with respect to both axes (see the third panels in Figure 4).

For the fluting mode ($m = 3$), $C_{2n+1}(s, m_{0i}^2)c_{2n+1}(\phi, m_{0i}^2)$ represents the solution along the major axis. Since $c_{2n+1}(\phi, m_{0i}^2) = -c_{2n+1}(\pi \pm \phi, m_{0i}^2)$, the density perturbation is symmetric about the major axis but it is asymmetric about the minor axis (see the fourth panel in Figure 5). $S_{2n+1}(s, m_{0i}^2)s_{2n+1}(\phi, m_{0i}^2)$ represents the solution of fluting waves perturbed along the minor axis. Since $s_{2n+1}(\phi, m_{0i}^2) = \mp s_{2n+1}(\pi \pm \phi, m_{0i}^2)$, the density perturbation is asymmetric about the major axis and symmetric about the minor axis (see the fourth panel in Figure 4).

3.2. Photospheric Conditions

Adapting this model to consider realistic physical plasma conditions of a sunspot under photospheric conditions, it is assumed that internal plasma temperature, density, and pressure are less than external values of their corresponding parameters, and internal magnetic field strength is greater than its external value. This leads to the following relations between the characteristic plasma speeds: $v_{Ai}, c_{Se} > c_{Si}, v_{Ae}$. These conditions are needed for surface waves to occur. For example, if the internal plasma is cooler than the external plasma, these conditions allow a fast surface wave to propagate with a phase

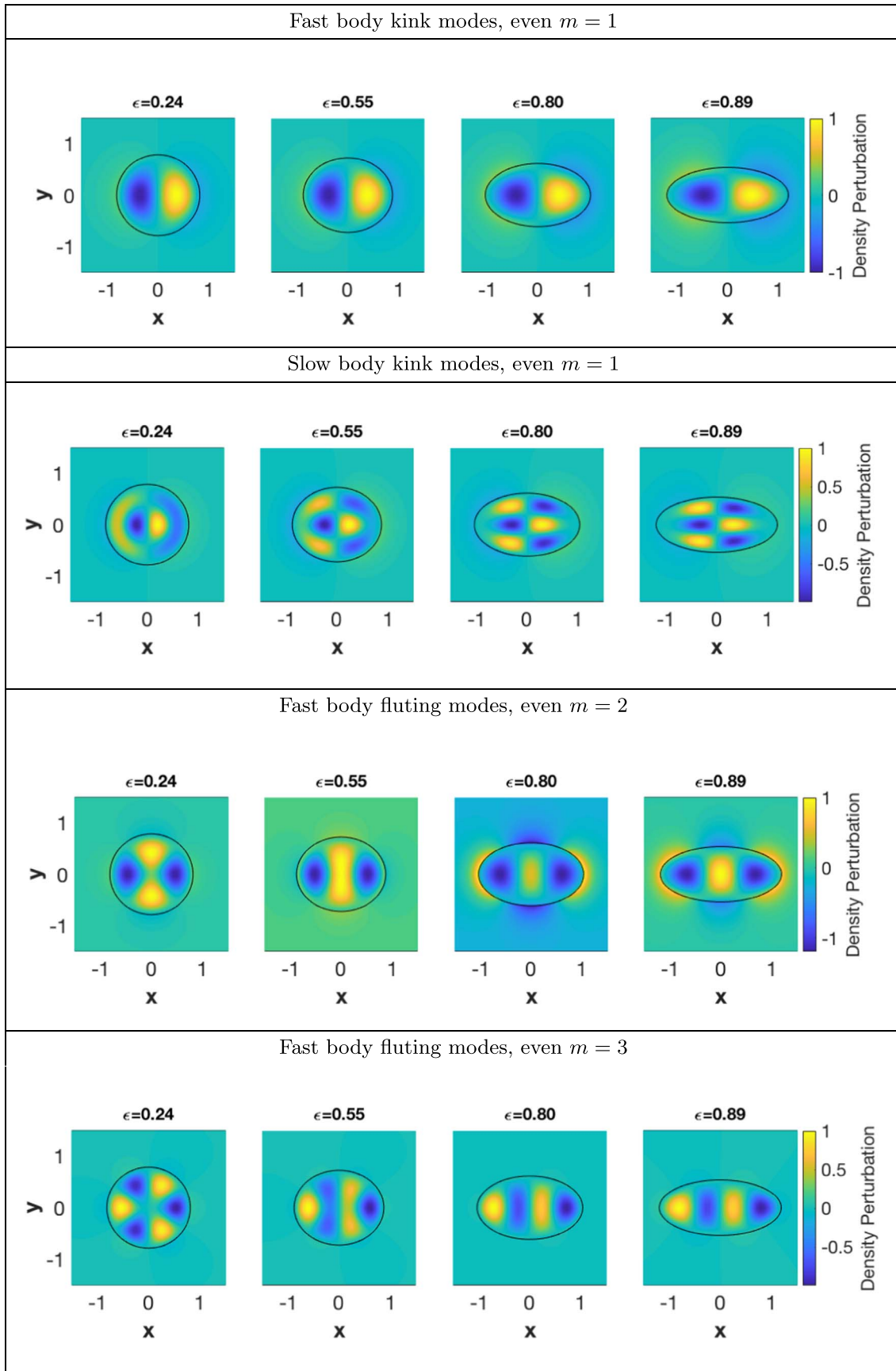


Figure 5. The normalized density perturbations under solar corona conditions, i.e., $v_{Ae}, v_{Ai} > c_{Si}, c_{Se}$ for the different values of eccentricity. From the top to the bottom, we show the fast branch of the kink mode, which has one hyperbola node and one ellipse node; the fast branch of the kink mode, which has one hyperbola node and two ellipse nodes; the fast branch of the fluting $m = 2$ mode, which has two hyperbola nodes and one ellipse node; the fast branch of the fluting $m = 3$ mode, which has three hyperbola nodes and one ellipse node, i.e., the even solution of the Mathieu equation.

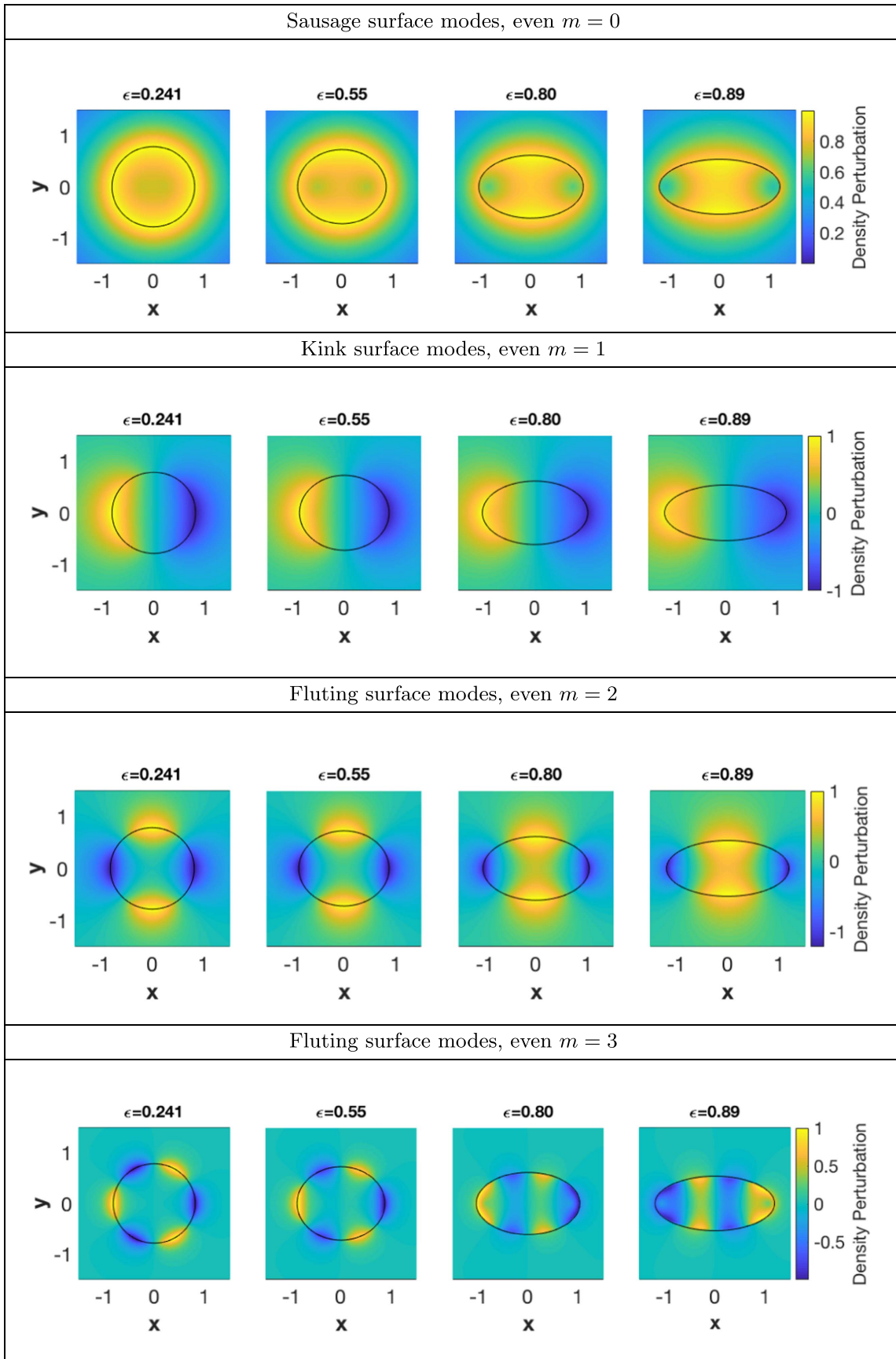


Figure 6. The normalized density perturbation under photospheric conditions, i.e., $v_{Ais}, c_{Ssc} > c_{Sis}, v_{Ae}$ for different values of eccentricity. From the top to bottom in the corresponding panels we show the fast surface branch of the sausage mode; the fast surface branch of the kink mode; the fast surface branch of the fluting $m = 2$ mode; the fast surface branch of the fluting $m = 3$ mode, i.e., the even solution of the Mathieu equation.

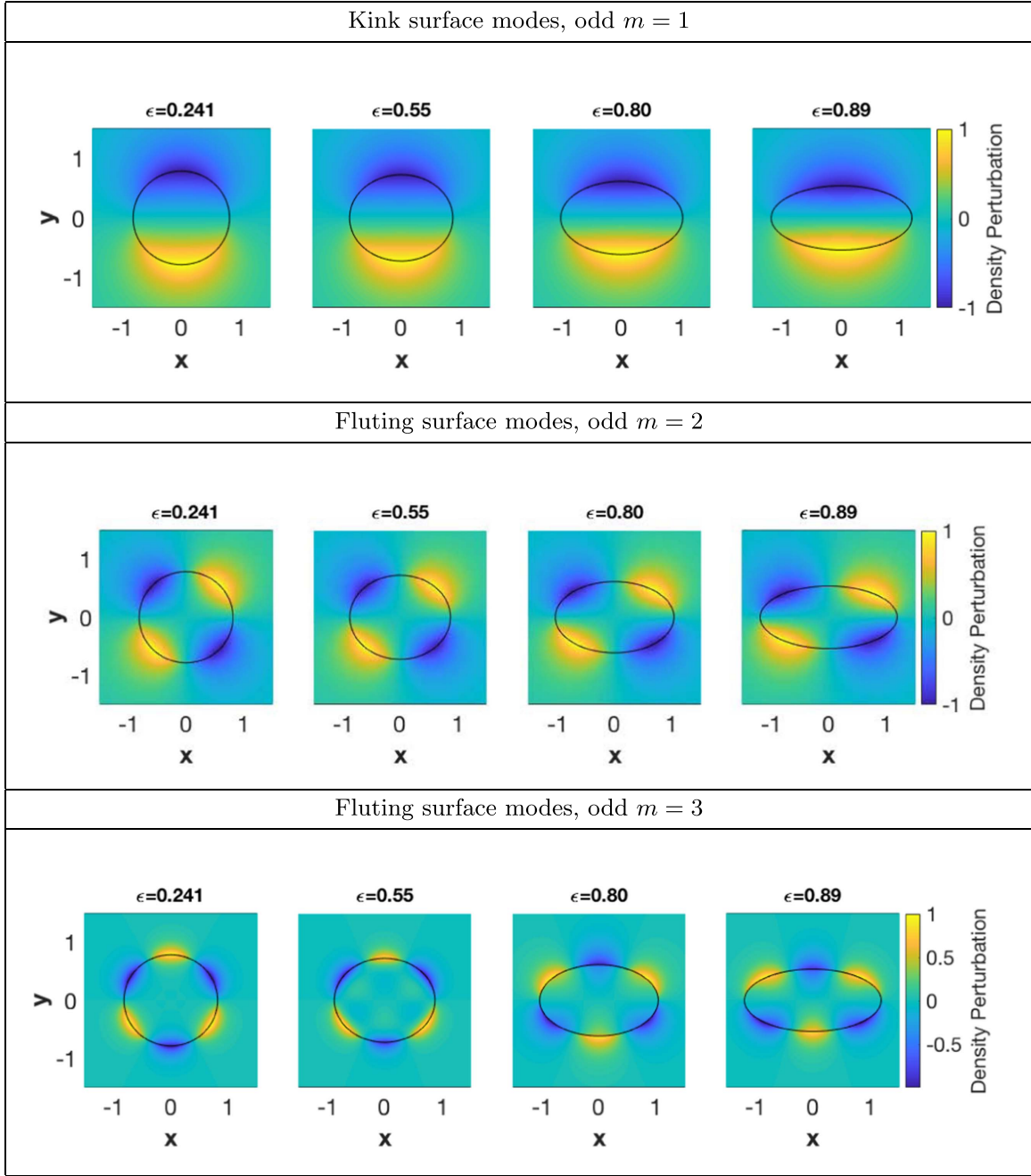


Figure 7. The normalized density perturbation under photospheric conditions, i.e., $v_{Ai}, c_{Se} > c_{Si}, v_{Ae}$ for different values of eccentricity. From the top to bottom on the corresponding panels, we show the fast surface branch of the kink mode; the fast surface branch of the fluting $m = 2$ mode; the fast surface branch of the fluting $m = 3$ mode, i.e., the odd solution of Mathieu equation.

speed of c_{Se} . If the internal magnetic field strength is greater than external value, these conditions will allow a slow surface mode with a phase speed equal to c_{Ti} . For the numerical calculations, we used the following ratios: $c_{Si} = 1$, $v_{Ae} = 0.5c_{Si}$, $c_{Se} = 1.5c_{Si}$, and $v_{Ai} = 2c_{Si}$. The total pressure balance between the internal and external plasma requires $\frac{\rho_e}{\rho_0} = 1.76$. Since, for the slow body mode $m_{0i}^2 > 0$ and $m_{0e}^2 < 0$, the dispersion Equation (19) was applied. $m_{0i}^2 < 0$ and $m_{0e}^2 < 0$ correspond to the slow surface mode, and therefore, the dispersion Equation (20) is applied for the surface wave. In addition, the dispersion relation given by Equation (20) was used for the

fast surface wave, which has a phase speed between the kink speed $c_k = \sqrt{(\rho_i v_{Ai}^2 + \rho_e v_{Ae}^2) / (\rho_i + \rho_e)}$ and c_{Se} .

In the next section, specific attention is paid to the fast surface mode, as the slow body mode is similar to what has been investigated previously under coronal conditions. The symmetrical properties will not be discussed as they have already been presented in Section 3.1.

3.2.1. Sausage Mode

The values used for the visualization of this mode are shown in Table 5. The fast surface sausage mode is presented in the

first panel in Figure 6. All four modes have the same wavelength, but have been calculated for different values of the ellipticity, (ϵ), of the cross section of the magnetic flux tube. The first panel in Figure 6 shows the density perturbations that correspond to the sausage mode. As discussed before, the fundamental sausage mode is only very slightly affected by altering the ellipticity. Therefore, the identification of the surface fundamental sausage mode is easier. For example, from the first panel in Figure 6, one can see that as ellipticity increases, the surface sausage mode can be identified more easily.

3.2.2. Kink Mode

The second panel in Figure 6 illustrates the density perturbation of the kink mode polarized along the major axis with differing values of eccentricity in an elliptic tube, while the first panel in Figure 7 illustrates the kink mode polarized along the minor axis. The parameters used for these calculations are presented in Table 5. The eccentricity of the flux tube does not affect the appearance of the kink surface mode as we only have fundamental kink surface modes unlike the body kink mode, which is affected by the ellipticity of tube when we have higher order kink modes. Therefore, it is possible to observe both kink surface modes in the photosphere even if the eccentricity is large.

3.2.3. Fluting Modes

The third and fourth panels in Figure 6 represent the density perturbation of the fluting modes $m=2$ and $m=3$, respectively. Both are perturbed along the major axis. The second and third panels in Figure 7 represent the density perturbation that corresponds to the fluting modes for $m=2$ and $m=3$, which are perturbed along the minor axis (see the parameters used for these calculations in Table 5). The fluting surface modes that are perturbed along the major axis exhibit the same behavior as the fluting body modes perturbed along the major axis. It is difficult to determine the type of the mode other than the fluting surface modes perturbed along the minor axis. The second and third panels in Figure 7 show the fluting modes $m=2$ and $m=3$ as the eccentricity increases. The third and fourth panels in Figure 6 show that identification of the fluting modes $m=2$ and $m=3$ is more difficult.

4. Conclusion

In this paper, MHD modes of a magnetic flux tube with an elliptical cross section embedded in a magnetic environment are discussed. The spatial structure of wave mode identification was studied under both photospheric and coronal solar conditions. Special attention was paid to the investigation of the effect of the eccentricity of a flux tube on the body modes under coronal and surface modes under photospheric conditions. The effect of the eccentricity of a flux tube varies according to the direction of the wave's polarization along the axes with order of modes and the type of wave observed (body or surface waves).

The higher order modes are strongly affected by the ellipticity of the flux tube when taking into account the direction of the polarized wave. Therefore, the higher order modes that polarized along the major axis are strongly affected by the ellipticity of the tube, while those that are polarized along the minor axis are very slight effected by ellipticity. The

eccentricity affects the wave modes polarized along the major axis in a way that makes the mode look like another type of mode. This can lead to misinterpreting the wave mode in observations. For example, as the ellipticity of the cross section of the flux tube increases, the fluting mode ($m=3$) may be misinterpreted as a kink mode ($m=1$). Also, it is evident that the sausage mode ($m=0$) cannot be easily identified (see Figure 3). As for the fundamental modes, they are not affected by altering the ellipticity of the flux tube and it is easy to identify the mode type independent of the axis of the perturbation, i.e., whether they are perturbed on the major or minor axis. For example, the overtone kink modes that are polarized along the major axis are more affected by ellipticity than the fundamental kink modes. The body waves with higher order modes that polarized along the major axis are affected by the ellipticity of the flux tube. In the case of surface waves, the fluting modes ($m > 1$) that are polarized along the major axis are only affected by the eccentricity of the flux tube. All surface and body wave modes that are polarized along the minor axis and all the fundamental surface and body wave modes that are polarized along the minor and major axis are less sensitive to ellipticity. Despite the influence of ellipticity on the wave modes, we can identify the patterns by looking at the properties of the symmetry and the number of elliptical and hyperbolic nodes.

It is also worth mentioning that other effects, such as longitudinal stratification, may affect both eigenfrequencies and the longitudinal eigenfunctions of the magnetic flux tube. Several studies of magnetic flux tubes with circular cross sections have been devoted to this problem in a thin flux tube approximation (see, e.g., Andries et al. 2005, 2009; Dymova & Ruderman 2006; Verth & Erdélyi 2008; Soler et al. 2011). It was shown that longitudinal density stratification modulates the amplitude of the perturbations with height, depending on the chosen z variation in density, e.g., if the density decreases with height, the amplitude of the perturbations will increase with height and the longitudinal wavelength will increase with height. Assuming that the variables can be separated, longitudinal stratification will not affect the spatial structure of the eigenfunctions in the x, y plane at a given height. However, the spatial structure of the eigenfunctions in the x, y plane will change with height if the cross-sectional shape changes with height.

The obtained results can be useful for the interpretation of upcoming high-resolution observations, e.g., DKIST and Solar Orbiter, as they can be used for the validation of MHD waveguides with noncircular cross sections. This paper will help both theorists and observers understand how the spatial structure of the purely real eigenmodes are distorted from the well-known circular flux tube model when ellipticity is considered. The study of the spatial structure of the MHD wave modes highlighted in this paper opens a whole new avenue in understanding waves observed in localized magnetic structures in the Sun's atmosphere.

A.A. acknowledges the Deanship of Scientific Research (DSR), King Faisal University, Al-Hassa, KSA for the financial support under Nasher Track (grant No. 186354). V.F. and G.V. thank The Royal Society International Exchanges Scheme for collaborations with Chile (IE170301) and Brazil (IES/R1/191114); the Science and Technology Facilities Council (STFC) grant ST/V000977/1. G.V. and V.F. would also like

to thank the International Space Science Institute (ISSI) in Bern, Switzerland, for the hospitality provided to the members of the team on ‘‘Toward Dynamic Solar Atmospheric Magneto-Seismology.’’ G.V. and D.B.J. wish to acknowledge scientific discussions with the Waves in the Lower Solar Atmosphere (WaLSA) team, which is supported by the Research Council of Norway (project No. 262622) and the Royal Society (award No. Hooke18b/SCTM). This research received financial support from the European Union’s Horizon 2020 research and innovation program under grant agreement No. 824135 (SOLARNET).

Appendix A

Power Series Expansions for Mathieu Functions in the Form of Trigonometric Series

The expansion of the Mathieu functions in the form of trigonometric series in the s direction are given below:

$$C_{2n}(s, m_0^2) = \sum_{r=0}^{\infty} A_{2r}^{2n} \cosh(2rs), \quad (22)$$

$$C_{2n+1}(s, m_0^2) = \sum_{r=0}^{\infty} A_{2r+1}^{2n+1} \cosh((2r+1)s), \quad (23)$$

$$S_{2n+1}(s, m_0^2) = \sum_{r=0}^{\infty} B_{2r+1}^{2n+1} \sinh((2r+1)s), \quad (24)$$

$$S_{2n+2}(s, m_0^2) = \sum_{r=0}^{\infty} B_{2r+2}^{2n+2} \sinh((2r+2)s). \quad (25)$$

The expansion of the Mathieu functions in the form of trigonometric series in the ϕ direction are given below:

$$c_{2n}(\phi, m_0^2) = \sum_{r=0}^{\infty} A_{2r}^{2n} \cos(2r\phi), \quad (26)$$

$$c_{2n+1}(\phi, m_0^2) = \sum_{r=0}^{\infty} A_{2r+1}^{2n+1} \cos((2r+1)\phi), \quad (27)$$

$$s_{2n+2}(\phi, m_0^2) = \sum_{r=0}^{\infty} B_{2r+2}^{2n+2} \sin((2r+2)\phi), \quad (28)$$

$$s_{2n+1}(\phi, m_0^2) = \sum_{r=0}^{\infty} B_{2r+1}^{2n+1} \sin((2r+1)\phi). \quad (29)$$

The coefficients A_{2r}^{2n} , A_{2r+1}^{2n+1} , B_{2r+1}^{2n+1} and B_{2r+2}^{2n+2} are related by the recurrence relations that can be obtained by substituting Equations (22)–(25) into Equation (10) or Equations (26)–(29) into Equation (9). The following recurrence relations among the expansion coefficients are given below.

A.1. Even–Even ($c_{2n}(\phi, m_0^2)$)

$$\begin{cases} hA_{ee}^{(0)} - m_0^2 A_{ee}^{(2)} = 0, \\ (h-4)A_{ee}^{(2)} - m_0^2 [2A_{ee}^{(0)} + A_{ee}^{(4)}] = 0, \\ [h - (2j)^2]A_{ee}^{(2j)} - m_0^2 [2A_{ee}^{(2j-2)} + A_{ee}^{(2j+2)}] = 0 \quad j = 2, 3, 4 \end{cases} \quad (30)$$

A.2. Even–Odd ($c_{2n+1}(\phi, m_0^2)$)

$$\begin{cases} (h-1)A_{eo}^{(1)} - m_0^2 [A_{eo}^{(1)} + A_{eo}^{(3)}] = 0, \\ [h - (2j+1)^2]A_{eo}^{(2j+1)} - m_0^2 [2A_{eo}^{(2j-1)} + A_{eo}^{(2j+3)}] = 0 \quad j = 2, 3, 4 \dots \end{cases} \quad (31)$$

A.3. Odd–Even ($s_{2n+2}(\phi, m_0^2)$)

$$\begin{cases} (h-4)B_{oe}^{(2)} - m_0^2 B_{oe}^{(4)} = 0, \\ [h - (2j)^2]B_{oe}^{(2j)} - m_0^2 [2B_{oe}^{(2j-2)} + B_{oe}^{(2j+2)}] = 0 \quad j = 2, 3, 4. \end{cases} \quad (32)$$

A.4. Odd–Odd ($s_{2n+1}(\phi, m_0^2)$)

$$\begin{cases} (h-1)B_{oo}^{(1)} - m_0^2 [B_{oo}^{(1)} + B_{oo}^{(3)}] = 0, \\ [h - (2j+1)^2]B_{oo}^{(2j+1)} - m_0^2 [2B_{oo}^{(2j-1)} + B_{oo}^{(2j+3)}] = 0 \quad j = 1, 2, 3, 4 \dots \end{cases} \quad (33)$$

Here, ee, eo, oe, and oo indexes indicate even–even, even–odd, odd–even, and odd–odd, respectively. For more details, see, e.g., Abramowitz & Stegun (1964), Arscott (1964), and McLachlan (1947).

Appendix B

Power Series Expansions for Mathieu Functions in Terms of Series of Bessel Functions of the First Kind

The expansions of the Mathieu functions in terms of series of Bessel functions of the first kind (J_m) are given below:

$$C_{2n}(s, m_0^2) = \frac{P_{2n}}{A_0^{2n}} \sum_{r=0}^{\infty} (-1)^r A_{2r}^{2n} J_r(v_1) J_r(v_2), \quad (34)$$

$$\begin{aligned} C_{2n+1}(s, m_0^2) &= \frac{P_{2n+1}}{A_1^{2n+1}} \sum_{r=0}^{\infty} (-1)^r A_{2r+1}^{2n+1} \\ &\times [J_r(v_1) J_{r+1}(v_2) + J_r(v_2) J_{r+1}(v_1)], \end{aligned} \quad (35)$$

$$\begin{aligned} S_{2n+1}(s, m_0^2) &= \frac{s_{2n+1}}{B_1^{2n+1}} \sum_{r=0}^{\infty} (-1)^r B_{2r+1}^{2n+1} \\ &\times [J_r(v_1) J_{r+1}(v_2) - J_r(v_2) J_{r+1}(v_1)], \end{aligned} \quad (36)$$

$$\begin{aligned} S_{2n+2}(s, m_0^2) &= -\frac{s_{2n+2}}{B_2^{2n+2}} \sum_{r=0}^{\infty} (-1)^r B_{2r+2}^{2n+2} \\ &\times [J_r(v_1) J_{r+2}(v_2) - J_r(v_2) J_{r+2}(v_1)]. \end{aligned} \quad (37)$$

Appendix C

The Non-oscillatory Case

For the non-oscillatory case, the parameters m_0^2 or m_e^2 in the Mathieu equation are negative. A change in the sign of the parameters m_0^2 or m_e^2 corresponds to the replacement of s by $(\frac{\pi i}{2} + s)$. By taking this into account, the Fourier series expansion corresponds to FeK_{2n} (for more details see Chapter 8 of McLachlan (1947)) when the parameter is positive is

$$C_{2n}(s_0, -m_e^2) = (-1)^n C_{2n}\left(\left(\frac{\pi i}{2} + s_0\right), m_e^2\right). \quad (38)$$

The expansions of the modified Mathieu functions in terms of series of Bessel functions of the first kind, (I_m), are given below:

$$C_{2n}(s, -m_0^2) = \frac{P'_{2n}}{A_0^{2n}} \sum_{r=0}^{\infty} (-1)^r A_{2r}^{2n} I_r(v_1) I_r(v_2), \quad (39)$$

$$C_{2n+1}(s, -m_0^2) = \frac{s'_{2n+1}}{B_1^{2n+1}} \sum_{r=0}^{\infty} (-1)^r B_{2r+1}^{2n+1} \times [I_r(v_1) I_{r+1}(v_2) + I_r(v_2) I_{r+1}(v_1)], \quad (40)$$

$$S_{2n+1}(s, -m_0^2) = \frac{P'_{2n+1}}{A_1^{2n+1}} \sum_{r=0}^{\infty} (-1)^r A_{2r+1}^{2n+1} \times [I_r(v_1) I_{r+1}(v_2) - I_r(v_2) I_{r+1}(v_1)], \quad (41)$$

$$S_{2n+2}(s, -m_0^2) = \frac{s'_{2n+2}}{B_2^{2n+2}} \sum_{r=0}^{\infty} (-1)^r B_{2r+2}^{2n+2} \times [I_r(v_1) I_{r+2}(v_2) - I_r(v_2) I_{r+2}(v_1)]. \quad (42)$$

Appendix D

Power Series Expansions of the Modified Mathieu Functions of the Third Kind in Terms of Series of Modified Bessel Functions of the First Kind

The expansions of the modified Mathieu functions of the third kind in terms of series of modified Bessel functions of the first kind, (I_m), and the second kind, (K_m), are given below:

$$FeK_{2n}(s, -m_0^2) = \frac{P'_{2n}}{\pi A_0^{2n}} \sum_{r=0}^{\infty} A_{2r}^{2n} I_r(v_1) K_r(v_2), \quad (43)$$

$$FeK_{2n+1}(s, -m_0^2) = \frac{s'_{2n+1}}{\pi B_1^{2n+1}} \sum_{r=0}^{\infty} B_{2r+1}^{2n+1} \times [I_r(v_1) K_{r+1}(v_2) - K_r(v_2) I_{r+1}(v_1)], \quad (44)$$

$$GeK_{2n+1}(s, -m_0^2) = \frac{P'_{2n+1}}{\pi A_1^{2n+1}} \sum_{r=0}^{\infty} A_{2r+1}^{2n+1} \times [I_r(v_1) K_{r+1}(v_2) + K_r(v_2) I_{r+1}(v_1)], \quad (45)$$

$$GeK_{2n+2}(s, -m_0^2) = \frac{s'_{2n+2}}{\pi B_2^{2n+2}} \sum_{r=0}^{\infty} B_{2r+2}^{2n+2} \times [I_r(v_1) K_{r+2}(v_2) - K_r(v_2) I_{r+2}(v_1)]. \quad (46)$$

Here, $v_1 = |m_0| e^{-s}$, $v_2 = |m_0| e^s$ and

$$P'_{2n} = \frac{(-1)^n c_{2n}(0, m_0^2) c_{2n}(\frac{\pi}{2}, m_0^2)}{A_0^{2n}} = (-1)^n P_{2n},$$

$$P'_{2n+1} = \frac{(-1)^{n+1} c_{2n+1}(0, m_0^2) c'_{2n+1}(\frac{\pi}{2}, m_0^2)}{m_0 A_1^{2n+1}} = (-1)^n P_{2n+1},$$

$$s'_{2n+1} = \frac{(-1)^n s'_{2n+1}(0, m_0^2) s_{2n+1}(\frac{\pi}{2}, m_0^2)}{m_0 B_1^{2n+1}} = (-1)^n s_{2n+1},$$

$$s'_{2n+2} = \frac{(-1)^{n+1} s'_{2n+2}(0, m_0^2) s'_{2n+2}(\frac{\pi}{2}, m_0^2)}{m_0^2 B_2^{2n+2}} = (-1)^{n+1} s_{2n+2}.$$

Appendix E

Dispersion Diagrams and Parameters Chosen

The different values of eccentricity (ϵ) for every case mode and fixed normalized wavenumber k_{s_0} were chosen to show the dependence of the normalized phase speed $v_{\text{PH}} = v_{\text{ph}}/c_{S_i}$ (c_{S_i} is the internal sound speed) on the shapes discussed. In particular, values of eccentricity of 0.241, 0.55, 0.80, and 0.89 correspond to the transition from a circular cross section to an elliptical cross section (see Tables 4 and 5). For the numerical calculations, we used the fixed normalized value of the elliptical sunspot area (A) to maintain the smooth transition from the circle to the ellipse and to be able to explore the modification of the wave modes. In addition to the modes shown in Figures 3–7, corresponding videos of these figures are currently available online at <http://pdg.group.shef.ac.uk/Visualisations.html>. The dispersion diagrams obtained under coronal and photospheric conditions are shown in Figures 8 and 9.

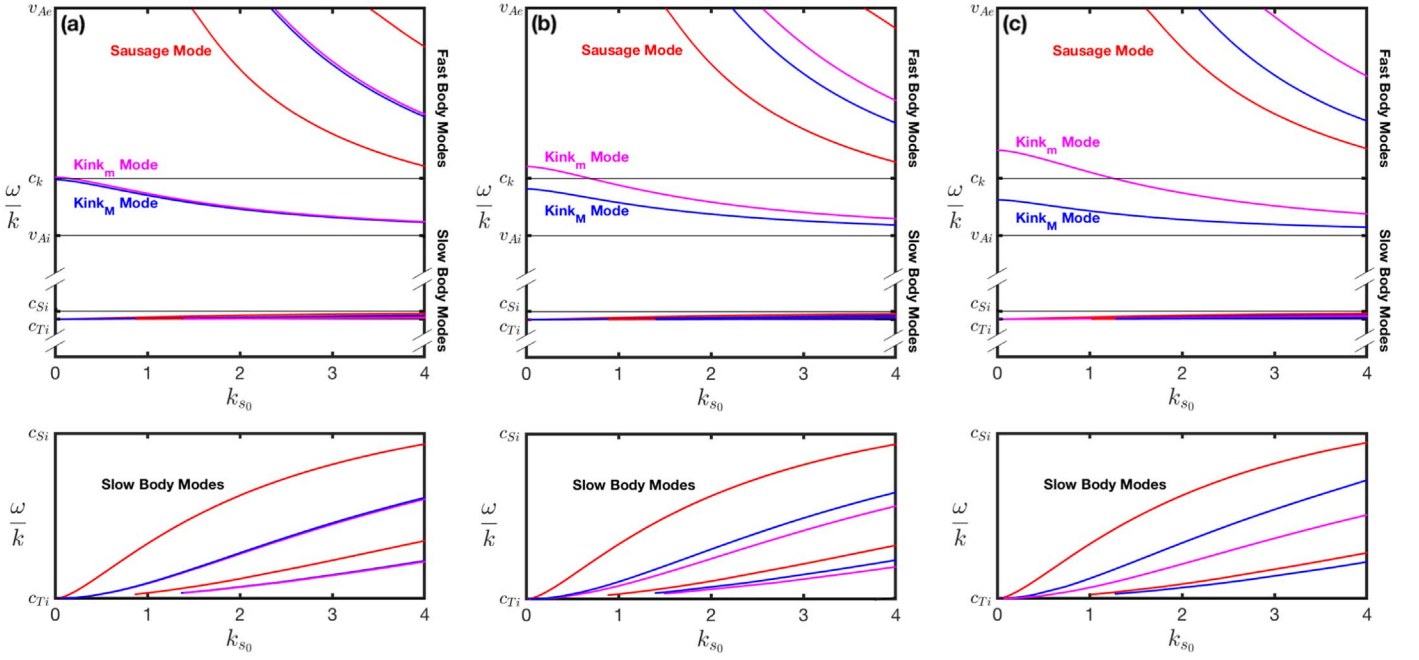


Figure 8. The phase speed (ω/k) of slow and fast body modes are shown under coronal conditions. Panels (a), (b), and (c) correspond to the different values of eccentricity of the cross section of the magnetic flux tube, i.e., $\epsilon = 0.24$ ($s_0 = 2.1$), $\epsilon = 0.65$ ($s_0 = 0.99$), and $\epsilon = 0.84$ ($s_0 = 0.60$). The bottom panels show a zoom-in of the corresponding regions from the panels above. The blue curves on all plots show the kink modes polarized along the major axis of the elliptical cross section of the magnetic flux tube (indicated as M as an index), the magenta curves represent the kink modes polarized along the minor axis (indicated as m as an index), and the red curves represent the sausage modes.

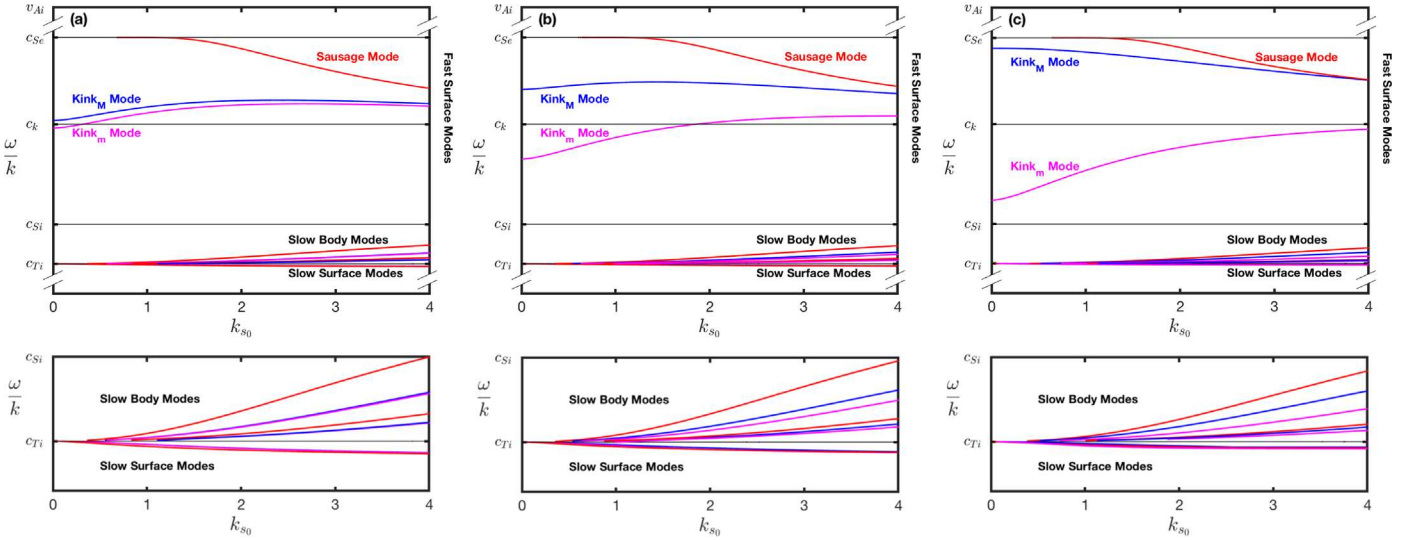


Figure 9. The phase speed (ω/k) of slow body and surface modes and fast surface modes are shown under photospheric conditions. Panels (a), (b), and (c) correspond to the different values of eccentricity of the cross section of the magnetic flux tube, i.e., $\epsilon = 0.24$ ($s_0 = 2.1$), $\epsilon = 0.65$ ($s_0 = 0.99$), and $\epsilon = 0.84$ ($s_0 = 0.60$). The bottom panels show a zoom-in of the corresponding regions from the panels above. The blue curves on all plots show the kink modes polarized along the major axis of the elliptical cross section of the magnetic flux tube (indicated as M as an index), the magenta curves represent the kink modes polarized along the minor axis (indicated as m as an index), and the red curves represent the sausage modes.

ORCID iDs

Gary Verth  <https://orcid.org/0000-0002-9546-2368>
 David B. Jess  <https://orcid.org/0000-0002-9155-8039>
 Viktor Fedun  <https://orcid.org/0000-0002-0893-7346>

References

- Abramowitz, M., & Stegun, I. 1964, Handbook of Mathematical Functions (Gaithersburg, MD: National Bureau of Standards)
- Albidah, A. B., Brevis, W., Fedun, V., et al. 2021, *RSPTA*, **379**, 20200181
- Alfvén, H. 1942, *Natur*, **150**, 405
- Andries, J., Arregui, I., & Goossens, M. 2009, *A&A*, **497**, 265
- Andries, J., Goossens, M., Hollweg, J. V., Arregui, I., & Van Doorselaere, T. 2005, *A&A*, **430**, 1109
- Arscott, F. M. 1964, *QJMat*, **15**, 103
- Aschwanden, M. J. 2005, Physics of the Solar Corona. An Introduction with Problems and Solutions (2nd ed.; Chichester: Praxis)
- Ballai, I., Forgács-Dajka, E., & Douglas, M. 2011, *A&A*, **527**, A12
- Bateman, H. 1955, Higher Transcendental Functions (New York: McGraw-Hill)
- Cally, P. S. 1986, *SoPh*, **103**, 277

- Cheremnykh, O., Fedun, V., Ladikov-Roev, Y., & Verth, G. 2018, *ApJ*, **866**, 86
- Cheremnykh, O. K., Fedun, V., Kryshal, A. N., & Verth, G. 2017, *A&A*, **604**, A62
- Cowling, T. G. 1976, *Magnetohydrodynamics* (Bristol: Adam Hilger)
- Cram, L. E., & Wilson, P. R. 1975, *SoPh*, **41**, 313
- Dymova, M. V., & Ruderman, M. S. 2006, *A&A*, **457**, 1059
- Edwin, P. M., & Roberts, B. 1983, *SoPh*, **88**, 179
- Erdélyi, R., & Fedun, V. 2006, *SoPh*, **238**, 41
- Erdélyi, R., & Fedun, V. 2007, *SoPh*, **246**, 101
- Erdélyi, R., & Fedun, V. 2010, *SoPh*, **263**, 63
- Erdélyi, R., & Morton, R. J. 2009, *A&A*, **494**, 295
- Fedun, V. 2008, in 37th COSPAR Scientific Assembly (Noordwijk: ESA), 864
- Giagkiozis, I., Goossens, M., Verth, G., Fedun, V., & Van Doorselaere, T. 2016, *ApJ*, **823**, 71
- Goedbloed, J. P. H., & Poedts, S. 2004, *Principles of Magnetohydrodynamics* (Cambridge: Cambridge Univ. Press)
- Goossens, M., Soler, R., Terradas, J., Van Doorselaere, T., & Verth, G. 2014, *ApJ*, **788**, 9
- Goossens, M. L., Arregui, I., & Van Doorselaere, T. 2019, *FrASS*, **6**, 20
- Hornsey, C., Nakariakov, V. M., & Fludra, A. 2014, *A&A*, **567**, A24
- Jess, D. B., Mathioudakis, M., Christian, D. J., et al. 2010, *SoPh*, **261**, 363
- Jess, D. B., Morton, R. J., Verth, G., et al. 2015, *SSRv*, **190**, 103
- Jess, D. B., Van Doorselaere, T., Verth, G., et al. 2017, *ApJ*, **842**, 59
- Kang, J., Chae, J., Nakariakov, V. M., et al. 2019, *ApJL*, **877**, L9
- Keys, P. H., Morton, R. J., Jess, D. B., et al. 2018, *ApJ*, **857**, 28
- Lighthill, M. J. 1960, *RSPTA*, **252**, 397
- Liu, C., Xu, Y., Cao, W., et al. 2016, *NatCo*, **7**, 13104
- Magyar, N., Van Doorselaere, T., & Goossens, M. 2019, *ApJ*, **873**, 56
- Mather, J. F., Ballai, I., & Erdélyi, R. 2018, *A&A*, **610**, A56
- Mathieu, E. 1868, *J. Math. Pures Appl.*, **13**, 137
- McLachlan, N. 1947, *Theory and Application of Mathieu Functions* (Oxford: Oxford Univ. Press)
- Morse, P. M., & Feshbach, H. 1953, *Methods of Theoretical Physics* (New York: McGraw-Hill)
- Musielak, Z. E., Huang, P., & Ulmschneider, P. 2000, *A&A*, **362**, 359
- NIST 2020, NIST Digital Library of Mathematical Functions, Release 1.0.28 of 2020 September 15, <http://dlmf.nist.gov/>
- Parker, E. N. 1974, *SoPh*, **37**, 127
- Parker, E. N. 2004, *JFM*, **519**, 377
- Pascoe, D. J., & Nakariakov, V. M. 2016, *A&A*, **593**, A52
- Priest, E. 2014, *Magnetohydrodynamics of the Sun* (Cambridge: Cambridge Univ. Press)
- Roberts, B. 1981a, *SoPh*, **69**, 27
- Roberts, B. 1981b, *SoPh*, **69**, 39
- Ruderman, M., Terradas, J., & Jose-Luis Ballester, P. 2014, in 40th COSPAR Scientific Assembly (Noordwijk: ESA), E2.2-30-14
- Ruderman, M. S. 2003, *A&A*, **409**, 287
- Ruderman, M. S., & Roberts, B. 2006, *JPIPh*, **72**, 285
- Soler, R., Terradas, J., Verth, G., & Goossens, M. 2011, *ApJ*, **736**, 10
- Spruit, H. C. 1982, *SoPh*, **75**, 3
- Terradas, J., Andries, J., & Goossens, M. 2007, *SoPh*, **246**, 231
- Terradas, J., Oliver, R., & Ballester, J. L. 2005, *A&A*, **441**, 371
- Verth, G. 2007, *AN*, **328**, 764
- Verth, G., & Erdélyi, R. 2008, *A&A*, **486**, 1015
- Verth, G., & Jess, D. B. 2016, in *Low-Frequency Waves in Space Plasmas*, ed. A. Keiling, D.-H. Lee, & V. Nakariakov (Washington, DC: American Geophysical Union), 431
- Vickers, E., Ballai, I., & Erdélyi, R. 2018, *SoPh*, **293**, 139
- Wentzel, D. G. 1979, *A&A*, **76**, 20
- Williams, T., Taroyan, Y., & Fedun, V. 2016, *ApJ*, **817**, 92
- Wilson, P. R. 1981, *ApJ*, **251**, 756